Ab initio molecular dynamics investigation of the elastic properties of superionic Li$_2$O under high temperature and pressure

Yu He [1,2,3,*] Shichuan Sun [1,3] and Heping Li [1,3]

[1]*Key Laboratory of High-Temperature and High-Pressure Study of the Earth's Interior, Institute of Geochemistry,*
Chinese Academy of Sciences, Guiyang 550081, Guizhou, China
[2]*Center for High Pressure Science and Technology Advanced Research, Shanghai 201203, China*
[3]*University of Chinese Academy of Sciences, Beijing 100049, China*

Theoretical prediction on the elastic properties of superionic material is challenging due to the fast diffusion of cation/anion in the lattice. Here, we investigated the elastic properties of Li$_2$O at elevated temperature and pressure using *ab initio* molecular dynamics (AIMD). We observed the superionic transition above 1300 K, and the highly diffusive Li$^+$ leads to local structure change with significant influence on the elasticity of Li$_2$O. We successfully predicted the significant C_{11} softening above 1300 K, and the calculated elastic constants fit the previous experimental results very well. It suggests the anharmonic lattice vibration before superionic transition and the diffusion of Li$^+$ after superionic transition are very important for the prediction on the elastic properties, and the AIMD method is able to describe the superionic behavior accurately. In addition, we calculated the bulk and shear moduli, sound velocities, as well as elastic and sound velocity anisotropies. We found that the superionic state transition also leads to the weakening of the elastic and sound velocity anisotropies in Li$_2$O. Pressure has negative effect on the mobility of Li$^+$, which strengthens the elastic stiffening effect of superionic Li$_2$O with increasing pressure.

I. INTRODUCTION

Deuterium (D)-tritium (T) nuclear fusion is one of the important solutions to future energy challenges [1–3]. Due to the limited tritium source in nature, a tritium breeding blanket was adopted for the continuous production of tritium in the fusion reactor [3–5]. In the breeder blanket region, tritium can be generated through nuclear transmutation of lithium, and lithium ceramics are considered as breeder materials. Relevant properties of lithium ceramics such as Li$_2$O, Li$_2$TiO$_3$, LiAlO$_2$, Li$_2$ZrO$_3$, Li$_2$SiO$_3$, and Li$_4$SiO$_4$ are investigated both theoretically and experimentally [5–17].

These materials are also known as superionics. At the superionic state, Li ions become highly diffusive within static oxide framework exhibiting high ionic conductivity over 0.1 S m^1. As one of the simplest binary lithium ceramics, the Li$^+$ transport property of antifluorite Li$_2$O has been widely studied [18–27]. The increasing mobility of Li$^+$ in Li$_2$O at high temperature has been confirmed by the NMR, ionic conductivity, and single-crystal neutron diffraction experiments, and the superionic transition temperature were determined to be ∼1200 K [28,29]. Molecular dynamic (MD) simulations were adopted to calculate Li$^+$ diffusion coefficients in Li$_2$O at superionic state [8,21–26]. The experimental and calculated ionic conductivities show good consistence especially at high temperatures. Recently, nonequilibrium molecular dynamics

method was used to predict the low-temperature Li$^+$ diffusion behavior in Li$_2$O accurately [23].

Mechanical properties for Li$_2$O are also important in governing the deformation and fracture of the fuel during both normal operation and potential transients [30]. The fast diffusion of Li$^+$ changes the Li$^+$ distribution in the lattice, and thus affects the mechanical properties of the materials. Hull *et al.* measured the elastic constants of Li$_2$O in the temperature range 293–1603 K [7]. An anomalous sharp decrease in C_{11} above ∼1350 K was attributed to the fast diffusion of Li$^+$ in the lattice. Experimental studies on the elastic constants change at high temperatures are quite rare due to the difficulty in obtaining single-crystal samples. As a result, calculations based on density-function theory (DFT) were used to predict the elastic properties of materials at high pressures and temperatures [10,12,20]. However, accurate prediction on the elastic properties of Li$_2$O at high temperature is still quite a challenge. The quasi-harmonic Debye model was used to calculate the elastic constants of Li$_2$O at high temperature [12,20]. Although instability of the phonon mode was observed before superionic transition, this method ignored the structure change ascribed to the superionic transition, and thus failed to predict the C_{11} softening above ∼1350 K as observed by experimental study [7]. Gupta *et al.* [20] observed the significant decrease in C_{11} of Li$_2$O in their empirical potential model calculations, but there is still a gap between calculated and experimental results. Here, *ab initio* molecular dynamics (AIMD) method was adopted to study the elastic properties of Li$_2$O. The calculated elastic constants with increasing temperature are consistent with experimental results, and the

*heyu@mail.gyig.ac.cn

TABLE I. AIMD simulated density, lattice parameter, elastic constants, bulk modulus, shear modulus, elastic anisotropic factor, and Poisson's ratio of Li_2O at different temperatures and pressures.

P (GPa)	T (K)	ρ (g cm^3)	a (Å)	C_{11} (GPa)	C_{12} (GPa)	C_{44} (GPa)	B (GPa)	G (GPa)	A	ν
0.0	0	2.00	4.63	206.8	24.1	54.2	85.00	66.89	0.593	0.188
0.0	700	1.96	4.66	167.5	22.5	51.9	70.83	59.35	0.716	0.173
0.0	1000	1.91	4.71	151.8	17.0	46.6	61.93	54.04	0.692	0.162
0.0	1300	1.84	4.76	143	16.3	34.0	58.53	43.74	0.537	0.201
0.0	1400	1.81	4.79	121.2	17.1	32.3	51.80	39.14	0.621	0.198
0.0	1500	1.80	4.80	108.5	5.3	28.7	39.70	36.38	0.557	0.149
0.0	1600	1.77	4.83	97.7	17.0	32.3	43.90	35.31	0.801	0.183
0.0	1700	1.75	4.84	93.1	29.4	23.1	50.63	20.27	0.725	0.279
10.0	0	2.22	4.48	249.2	50.4	76.6	116.67	85.03	0.771	0.207
10.0	1000	2.08	4.50	205.0	40.1	53.9	95.27	64.04	0.654	0.225
10.0	1700	2.05	4.60	164.6	42.0	52.8	82.87	56.05	0.861	0.224
20.0	0	2.39	4.37	292.5	82.9	92.5	152.77	97.24	0.883	0.237
20.0	1000	2.35	4.39	254.4	77.9	69.0	136.73	76.15	0.782	0.265
20.0	1700	2.25	4.46	220.8	79.5	70.5	126.60	70.56	0.998	0.265
30.0	0	2.53	4.28	332.2	115.0	103.2	187.40	105.32	0.950	0.263
30.0	1000	2.50	4.30	295.1	106.0	87.3	169.03	90.13	0.923	0.273
30.0	1700	2.42	4.35	275.0	100.2	73.5	158.47	78.78	0.841	0.287

elastic anisotropy and sound velocities of Li_2O are studied upon superionic transition. Moreover, we predicted the elastic properties of Li_2O with increasing pressure in both solid and superionic states.

II. COMPUTATIONAL METHODS

A. Lattice relaxation and migration barrier energy calculations

Ab initio calculations were executed using the Vienna *Ab initio* Simulation Package (VASP) [31] based on the DFT [32,33]. The projected augmented wave potentials were used to deal with the electronic exchange-correlation interaction along with the PBE(Perdew-Burke-Ernzerhof)-GGA(generalized gradient approximation) functional [34,35]. A plane-wave representation for the wave function with a cutoff energy of 800 eV was applied. Geometry optimizations were performed by using a conjugate gradient minimization until all the forces acting on ions were less than 0.01 eV/Å per atom. The fully relaxed structure was treated as the structure at normal pressure. k-point mesh with a spacing of *ca*. 0.03 Å^{-1} was adopted. The structures at high pressures were obtained by the relaxation at 20, 50, and 100 GPa. The Li^+ migration barrier energy was calculated by the Climbing-Image Nudged Elastic Band (CINEB) method [36]. A larger 2×2×2 supercell containing 96 atoms was adopted for our simulation, and 9 images were duplicated in our calculations between the starting point and the end point of migrating ion to simulate the intermediate states. For the large supercell adopted in the CINEB calculations, only the gamma point was adopted for k-point sampling to reduce the computational cost. The convergence check indicated that a denser k mesh did not affect our conclusion.

B. Diffusion coefficients and ionic conductivities calculations

In AIMD calculations, 2×2×2 supercells containing 96 atoms were employed. The energy cutoff was reduced to 400 eV, which is energetically converged based on our cut-off energy test [37] (Fig. S1). Brillouin-zone sampling was performed at the Γ point. An equilibration step was first carried out in the canonical ensemble (constant N, V, T) using a Nosé thermostat [38]. The simulations are conducted at hydrostatic 0 to 30 GPa and temperatures from 700 to 1700 K with a time step of 1 fs lasting over 20 000 steps. The time-average mean-square displacements (MSD) of the different atoms were generated using the atomic configuration information from every finite MD time step, defined as

$$\langle [\vec{r}(t)]^2 \rangle = \frac{1}{N} \sum_{i=1}^{N} \langle [\vec{r}_i(t+t_0) - \vec{r}_i(t_0)]^2 \rangle, \qquad (1)$$

where $\vec{r}_i(t)$ is the displacement of the ith Li ion at time t, and N is the total number of Li^+ in the system. D is obtained by a linear fit to the time dependence of the average MSD. The obtained D at various temperatures can be fitted with the Arrhenius equation:

$$D = A\exp\left(-\frac{\Delta H}{kT}\right), \qquad (2)$$

where ΔH is the activation enthalpy, A is a pre-exponential factor, k is the Boltzmann constant, and T is the temperature. The electrical conductivity is calculated on the basis of the diffusion coefficients and the Nernst-Einstein equation:

$$\sigma = \frac{fDcq^2}{kT}, \qquad (3)$$

where σ is the electrical conductivity, f is a numerical factor approximately equal to unity, D is the diffusion coefficient, c is the concentration of Li^+, q is the electrical charge, k is the Boltzmann constant, and T is the temperature. Additional computational details can be found in our previous works [39,40].
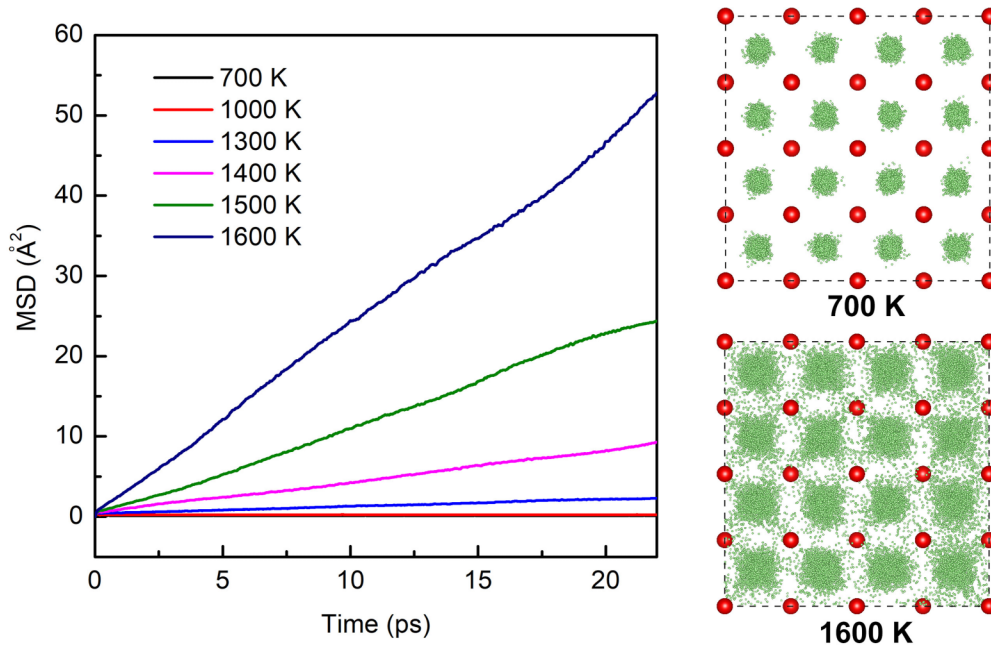
FIG. 1. MSDs of Li^+ in Li_2O at different temperatures. The trajectories of Li^+ at 700 and 1600 K are shown with small green balls in the lattices. Oxygen atoms are represented by red spheres.

C. AIMD elastic constants calculations at high temperatures

To calculate the elastic constants, it is important to generate the structures at hydrostatic pressure and different temperatures [41,42]. We determined the equilibrium volume and cell parameter at different temperatures by conducting a grid of NVT ensemble simulations over volumes and temperatures. For each equilibrium structure at different temperature, a 20 000 time-step (20 ps) simulation was conducted to check for sure that the stress field is hydrostatic. The elastic constant C_{ij} was calculated by distorting the equilibrium structure and solving the stress-strain relations.

The elastic properties of crystal are expressed as the relationship between stress and strain:

$$\sigma_{ij} = C_{ijkl}\varepsilon_{kl}, \tag{4}$$

where σ_{ij} refers to stress tensor, ε_{kl} refers to strain tensor, and C_{ijkl} represents fourth-order elastic modulus. Considering the symmetry of C_{ijkl}, the equation is simplified as below:

$$\sigma_i = C_{ij}\varepsilon_j. \tag{5}$$

The equation could be expanded as follows:

$$
\begin{pmatrix} \sigma_1 \\ \sigma_2 \\ \sigma_3 \\ \sigma_4 \\ \sigma_5 \\ \sigma_6 \end{pmatrix} =
\begin{pmatrix}
C_{11} & C_{12} & C_{13} & C_{14} & C_{15} & C_{16} \\
 & C_{22} & C_{23} & C_{24} & C_{25} & C_{26} \\
 & & C_{33} & C_{34} & C_{35} & C_{36} \\
 & & & C_{44} & C_{45} & C_{46} \\
 & & & & C_{55} & C_{56} \\
 & & & & & C_{66}
\end{pmatrix}
\times
\begin{pmatrix} \varepsilon_1 \\ \varepsilon_2 \\ \varepsilon_3 \\ \varepsilon_4 \\ \varepsilon_5 \\ \varepsilon_6 \end{pmatrix}. \tag{6}
$$

For the cubic system investigated in this work, we calculated the three nonequivalent elastic constants, C_{11}, C_{12}, and C_{44} can be obtained by a strain tensor:

$$
\varepsilon = \begin{pmatrix} \delta & 0 & 0 \\ 0 & 0 & 0 \\ 0 & 0 & 0 \end{pmatrix}, \tag{7}
$$

and we obtained C_{44} using a strain tensor:

$$
\varepsilon = \begin{pmatrix} 0 & 0 & 0 \\ 0 & 0 & \delta/2 \\ 0 & \delta/2 & 0 \end{pmatrix}, \tag{8}
$$

where δ is the magnitude of distortion. For δ in ± 0.01, ± 0.005, and 0, five group of strains were added by

$$a' = a(I + \varepsilon), \tag{9}$$

where a represents third-order cell parameter matrix, and ε represents added strain $\Delta\varepsilon$, I represents third-order identity matrix. In order to ensure the reliability and full convergence of the results, 10 000 time steps of NVT simulations were carried out for each direction of deformation. The final results of strain-stress data show very good linear relationship and were fitted to Eq. (4) employing the central difference method. For each optimizing result, the calculated correlation coefficient R^2 was larger than 99%.

D. Melting temperature estimation using coexistence method

We estimated the melting temperature of Li_2O using the coexistence method, which has been widely used to predict the melting temperatures of metals [43,44], hydrogen [45], and lithium hydride [46]. The coexistence model was constructed by combining a solid and liquid Li_2O structure. The solid structure was generated using a $4\times2\times2$ supercell containing 192 atoms, which was thermally equilibrated at
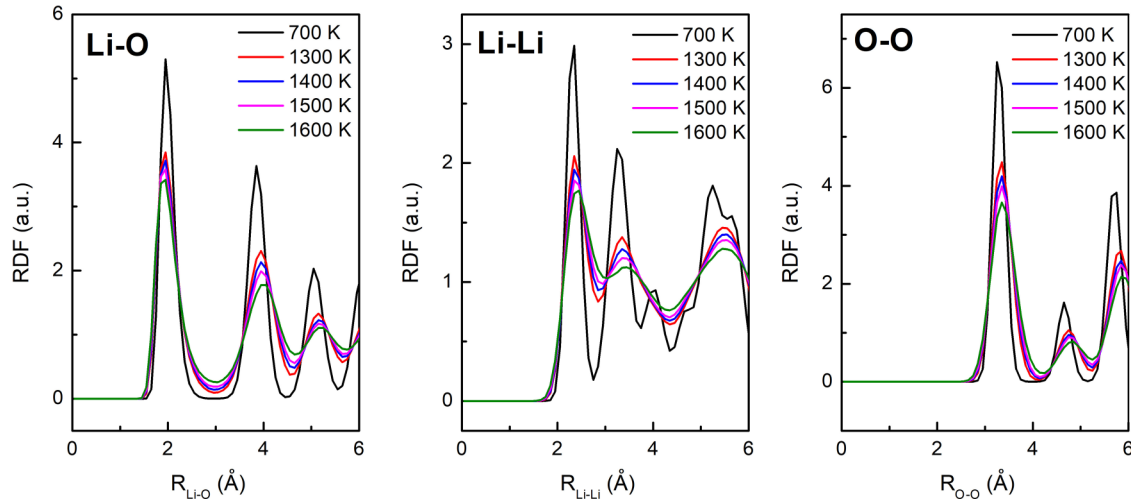
FIG. 2. RDF of Li-O, Li-Li, and O-O in Li_2O at 700, 1300, 1400, 1500, and 1600 K.

~1500 K for ~2 ps. The liquid structure was generated by heating the solid structure at ~5000 K for ~2 ps, and then slowly cooling down to ~1700 K. The AIMD simulation was performed on the coexistence model containing 384 atoms in the NVE (N-number of particles, V-volume, E-internal energy) ensemble. Under a constant internal energy, the co-existence system can be maintained for a long time, and the average temperature and pressure of the coexistence system

denotes a melting point. The cutoff energy was set to 400 eV with Γ point for k-space sampling. The time step was set at 1 fs with total simulation of over 18 ps. The coexisting state is maintained during our simulation (Fig. S2). The pressures and temperatures in the simulation are presented in Fig. S3, and averaged melting temperature for Li_2O is approximately 1673 ($\pm$50) K at 0.27 ($\pm$0.5) GPa [37].

III. RESULTS AND DISCUSSION

A. Superionic transition and local structural change

We conducted AIMD simulations on Li_2O at 700, 1000, 1300, 1400, 1500, and 1600 K. The cell parameter for each structure is adjusted to maintain hydrostatic normal pressure, thus the thermal expansion of the lattice is considered in our simulations. The lattice parameters and volumes at different temperatures are exhibited in Table I. The densities and cell parameters fit the experimental measurements very well (Fig. S4) [37]. At 700 K, Li^+ MSD does not increase with simulation time, and Li^+ simply vibrate about their lattice positions, indicating an ordinary solid state (Fig. 1). At temperatures above 1300 K, Li^+ diffuse off their lattice sites and the MSD increases with simulation time, while O ions show negligible displacement, suggesting a superionic state. It should be noted that superheating solid state can be obtained in AIMD simulation above the melting temperature [47,48]. The melting temperature of Li_2O was estimated by the coexistence method [37,47]. The selected simulated temperatures are lower than the estimated melting temperature of Li_2O (Fig. S3). The solid-superionic transition in Li_2O is considered as the second-order phase transition due to the continuous change of volume and discontinuous change of thermal expansion coefficient with increasing temperatures (Fig. S5) [37,49]. The diffusion coefficients of Li^+ can be deduced from the MSDs over time at different temperatures, and are consistent with previous experimental and molecular dynamics simulation results [8,18]. The diffusion coefficient at 1600 K is $\sim 1 \times 10^{-4.5}$ cm^2 s^{-1}. The diffusion coefficients are fitted through the Arrhenius equation at temperatures varying from 1300 to 1600 K, and the estimated diffusion activation enthalpy is 1.98 eV. Using the Nernst-Einstein equation,
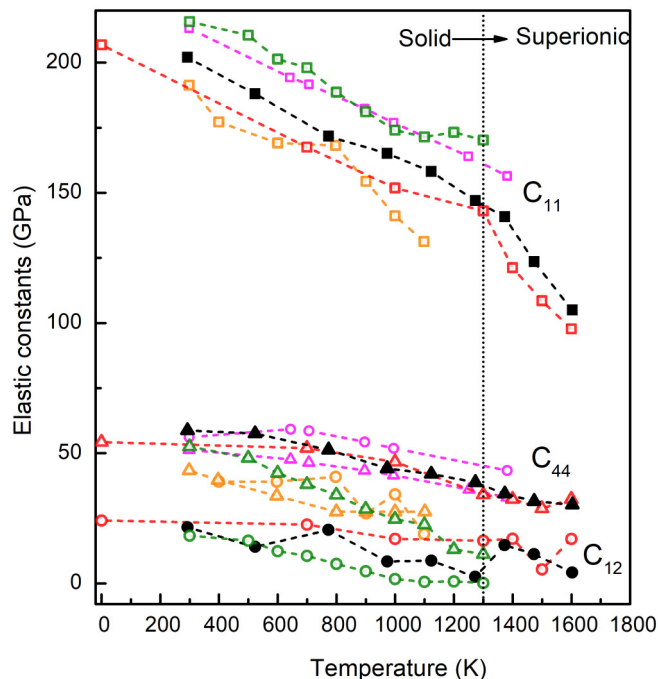

FIG. 3. The elastic constants of Li_2O at temperatures from 0–1600 K. The data of this study calculated by AIMD simulations are presented by red symbols compared with the results of experimental measurements (black solid symbols) [7] and quasi-harmonic calculations (green [12] and magenta [20] symbols). The orange symbols represent the calculated values using empirical potential MD simulations [20]. The elastic constants for C_{11}, C_{12}, and C_{44} are displayed with squares, circles, and triangles, respectively.
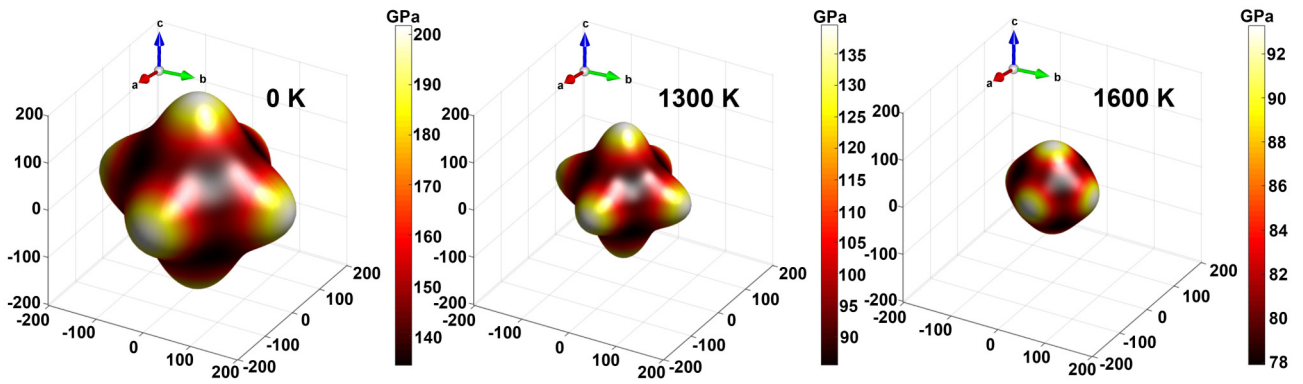
FIG. 4. 3D directional dependence of the elastic anisotropy of Young's modulus of Li_2O at the temperature of 0, 1300 and 1600 K.
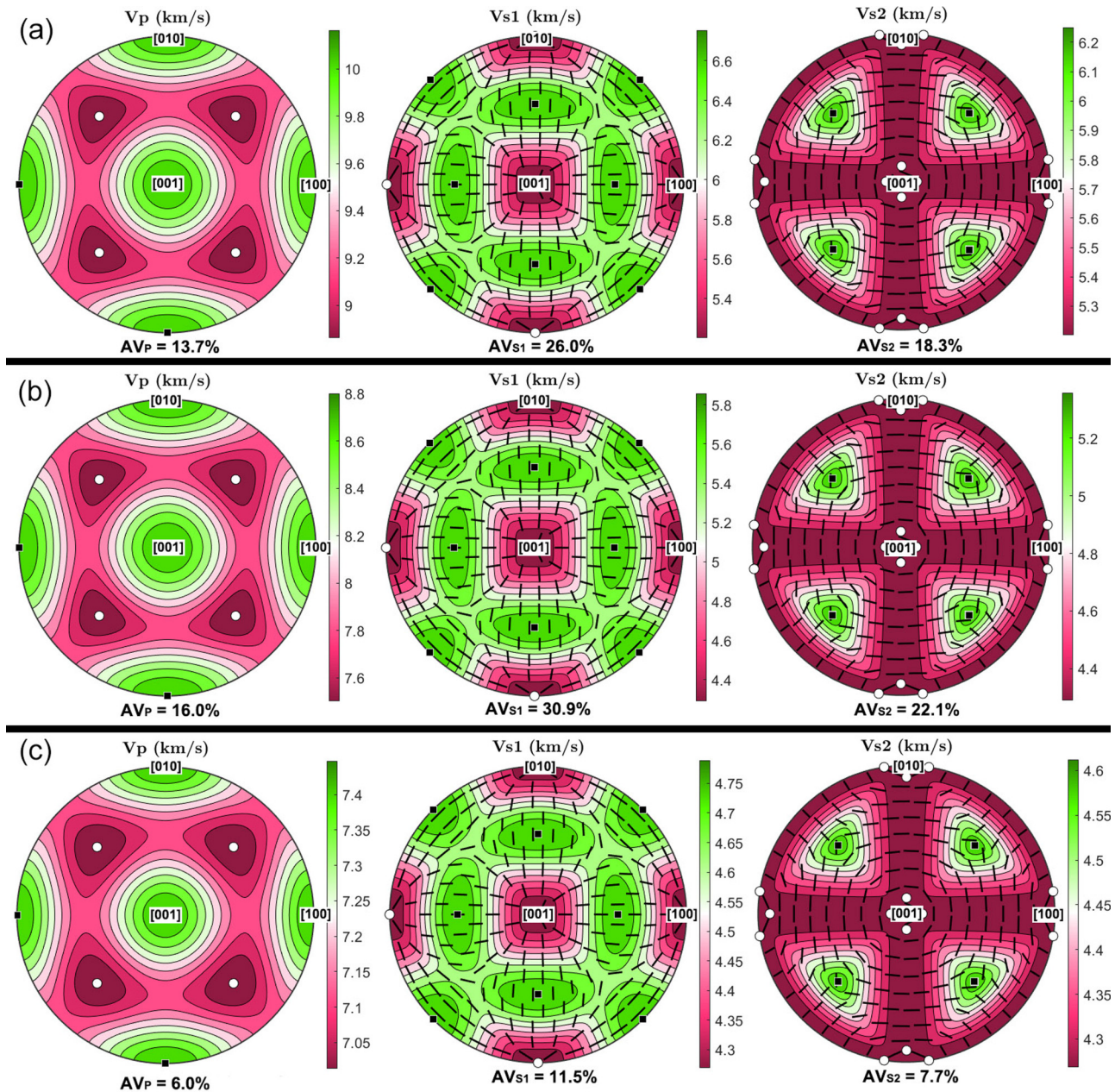

FIG. 5. Sound velocity anisotropies of V_P and two split shear-wave velocities V_{S1} and V_{S2} in Li_2O at (a) 0 K, (b) 1300 K, and (c) 1600 K, employing MTEX [54].
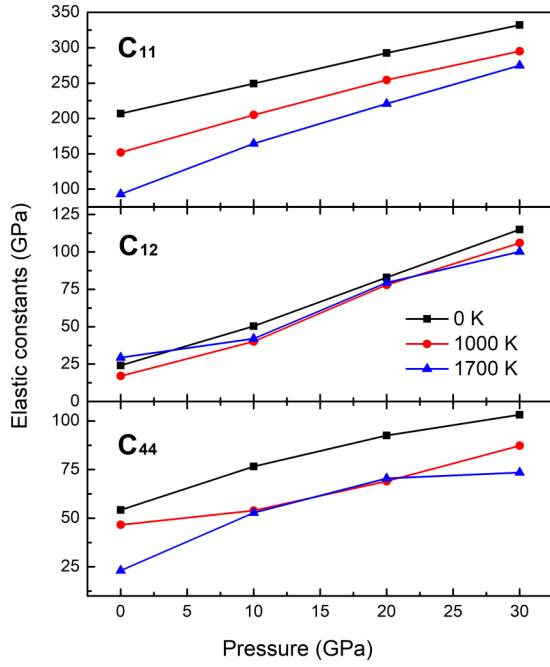
FIG. 6. The evolution of Li_2O elastic constants C_{11}, C_{12}, and C_{44} with increasing pressure. The elastic constants calculated at 0, 1000, and 1700 K are shown with black, red, and blue symbols.

we calculated the Li^+ conductivities and plotted them in Fig. S6 [37]. The ionic conductivity of Li_2O increases rapidly with temperature, and reaches 268 S m^{-1} at 1600 K.

The transition from ordinary solid state to superionic state in Li_2O at ~1300 K leads to significant increase in electric conductivity, and the Li^+ distribution change in the lattice (Fig. 1). Radial distribution functions (RDFs) of Li-O, Li-Li, and O-O at various temperatures are compared in Fig. 2, indicating local structure changes with the increasing temperature. The superionic transition leads to the boarding of Li-O, Li-Li, and O-O distribution. Especially, the Li-Li RDFs are much more homogeneous at the superionic state. The obvious diffusion of Li^+ may bring significant influence on the elastic properties, which are investigated by the AIMD method.

B. Elastic properties

Using the AIMD method, we obtained the hydrostatic high-temperature structures of Li_2O. We conducted a series of simulations on the distorted equilibrium structures and solved the stress-strain relation to obtain the elastic constants C_{ij} of Li_2O at high temperatures. For face-centered-cubic Li_2O, there are three independent elastic constants (C_{11}, C_{12}, and C_{44}) as shown in Fig. 3. The calculated elastic constants satisfy Born's stability conditions [Eq. (10)], indicating these high-temperature structures are mechanically stable.

$$C_{11} - C_{12} > 0, \quad C_{11} + 2C_{12} > 0, \quad C_{44} > 0 \quad (10)$$

The calculated elastic constants are compared with previous experimental and computational results (Fig. 3). Our results show quite good consistence with previous experimental study. We observed the significant softening of C_{11} at temperatures above ~1300 K, and this effect can be attributed

to the local structure change of Li_2O due to the obvious Li^+ diffusion. The change of C_{12} and C_{44} upon the superionic transition is marginal. The instability of phonon mode of Li_2O was reported at the temperature before superionic transition, which makes the prediction of elastic constants at superionic state impossible for quasi-harmonic method [20]. Our results fit the experimental data better than previous quasi-harmonic prediction even at low temperatures [12]. It suggests anharmonic vibration in the lattice because the high mobility of Li^+ is significant in Li-bearing materials even before the superionic transition. MD simulation with empirical potential is able to predict the elastic softening behavior of Li_2O at superionic state. However, the softening temperature is about 500 K lower than experimental results. The AIMD method giving comparable results with experiments should be the most accurate theoretical approach to predict the elastic properties of superionic materials, which have the potential to be used as materials for breeder blanket, lithium-ion batteries, and solid oxide fuel cells.

The Voigt-Reuss-Hill scheme was used to estimate the elastic properties of polycrystalline Li_2O. The bulk and shear modulus are defined as

$$B = \frac{B_V + B_R}{2}, \quad G = \frac{G_V + G_R}{2}, \quad (11)$$

where B_V and G_V denote bulk and shear modulus within the Voigt model [50]. B_R and G_R denote bulk and shear modulus within the Reuss model [51]. These moduli were deduced with the calculated elastic constants:

$$B_V = B_R = \frac{(C_{11} + 2C_{12})}{3}; \ G_V = \frac{(C_{11} - C_{12} + 3C_{44})}{5};$$
$$G_R = \frac{5}{(4/(C_{11} - C_{12}) + 3/C_{44})}. \quad (12)$$

Young's modulus (E) and Poisson's ratio (ν) were deduced accordingly and shown in Table I [Eq. (13)]:

$$E = \frac{9BG}{B + 3G}; \quad \nu = \frac{3B - G}{2(3B + G)}; \quad (13)$$

To investigate the elastic anisotropy, the three-dimensional (3D) directional dependence of elastic modulus is studied using the following relation:

$$\frac{1}{E_\omega} = (1 - l_3^2)^2 s_{11} + l_3^4 s_{33} + l_3^2(1 - l_3^2)(2s_{13} + s_{44}), \quad (14)$$

where E_ω denotes Young's modulus of the direction ω. l_1, l_2, and l_3 are the directional cosines of ω. s_{11}, s_{13}, s_{33}, and s_{44} denote elastic compliance. The evolution of elastic anisotropy can be properly visualized using 3D directional dependence of Young's moduli at 0, 1300, and 1600 K (Fig. 4). Young's moduli are stronger along $\langle 100 \rangle$, $\langle 010 \rangle$, and $\langle 001 \rangle$ directions, and decrease with increasing temperature. Upon the superionic state transition above 1300 K, the significant reduction of C_{11} leads to the weakening of elastic anisotropy, and the 3D diagram at 1600 K is more homogeneous like a sphere. It suggests the highly diffusive Li^+ also affects the elastic anisotropy of Li_2O.
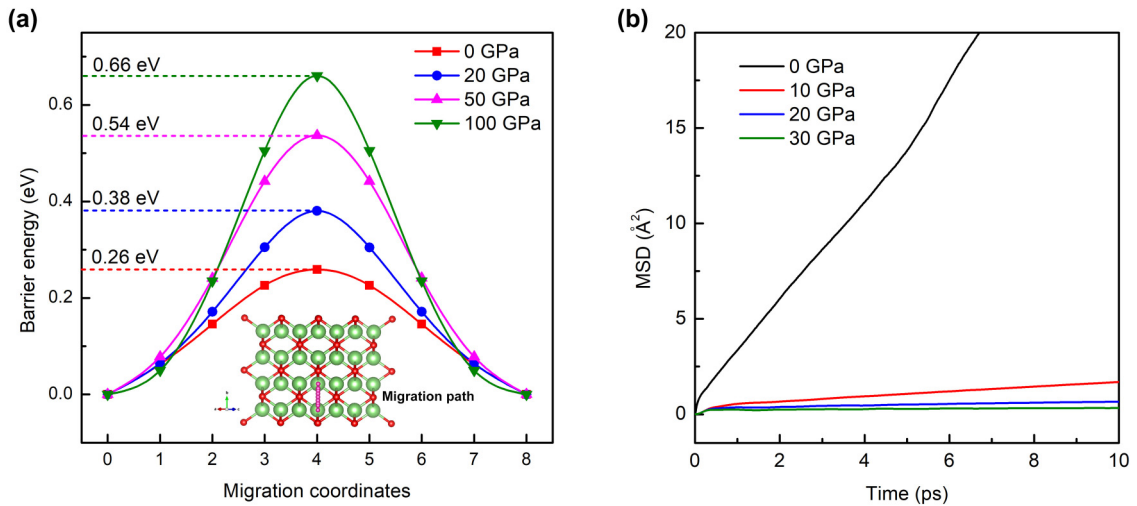
FIG. 7. The change of Li$^+$ transportation properties with increasing pressure. (a) Calculated barrier energies of Li$^+$ migration along $\langle 010 \rangle$ directions at normal and high pressures. The migration path is represented by purple balls in the inserted Li$_2$O lattice. Green and red spheres denote Li and O atoms. (b) MSDs of Li$^+$ in Li$_2$O at 1700 K and pressures from 0 to 30 GPa.

C. Sound velocities

With the calculated bulk and shear moduli, the compression (V_P), shear (V_S), and bulk (V_ϕ) velocities in polycrystalline Li$_2$O are obtained and shown in Table I and Fig. S7 [37]:

$$V_P = \sqrt{\frac{B + \frac{4G}{3}}{\rho}},$$

$$V_S = \sqrt{\frac{G}{\rho}}, \quad V_\emptyset = \sqrt{\frac{B}{\rho}}. \quad (15)$$

The decreases in V_P and V_ϕ are more significant than that of V_S upon the superionic transition above 1300 K. The sound velocities along different directions can be obtained by solving the Christoffel equation [52,53]:

$$|C_{ijkl} n_j n_l - \rho V^2 \delta_{ik}| = 0. \quad (16)$$

In high-symmetry directions, when polarization directions are parallel or vertical with the propagation directions of velocities, the modes are called pure longitudinal or transverse, respectively. In general directions, the velocities are divided into one quasi-longitudinal V_P (closet to propagation directions) and two spitting shear-wave velocities (V_{S1} and V_{S2}). The seismic anisotropy of P wave and S wave are defined as

$$AV = \frac{(V^{MAX} - V^{MIN}) \times 200}{(V^{MAX} + V^{MIN})}, \quad (17)$$

where V^{MAX} and V^{MIN} are the maximum and minimum velocities. The velocities along lattice directions are exhibited by the circular patterns (Fig. 5). From 0 to 1300 K, the velocities decrease obviously, while the velocity anisotropies show slight increases. The AV_P, AV_{S1}, and AV_{S2} in superionic Li$_2$O at

1600 K are 6.0, 11.5, and 7.7%, respectively, which are quite low compared with those at 1300 K.

D. Elasticity at high pressure

We performed AIMD simulations on Li$_2$O at high pressure to explore the pressure effect on the superionicity and elasticity. In the simulations, the volumes of supercells are finely adjusted to maintain hydrostatic pressures at 10, 20, and 30 GPa. The densities and cell parameters are presented in Table I. At high pressure, elastic constants are calculated at 0, 1000, and 1700 K and shown in Fig. 6. Generally, all the elastic constants increase with applied pressure, and still satisfy Born's stability conditions [Eq. (10)], indicating the elastic stabilization of Li$_2$O at high P-T (<30 GPa and <1700 K). With increasing pressure, the gap of C_{11} at 1000 and 1700 K is reduced. It suggests pressure may have significant influence on the Li$^+$ mobility, and the Li$^+$ transportation properties under high pressure are investigated. CINEB method was used to calculate the migration barrier energy of Li$^+$ along $\langle 010 \rangle$ directions by optimizing nine images between two nearest Li$^+$ tetrahedral sites [purple balls in the inset of Fig. 7(a)]. The barrier energy is 0.26 eV at normal pressure, which is consistent with previous study [20]. It is noted that the barrier energy calculated by CINEB method can be quite different comparing with the diffusion activation enthalpy (ΔH) calculated by AIMD simulations because of quite different migration paths at high temperature [20,55]. Upon compression, the migration barrier energy increases from 0.26 eV at 0 GPa to 0.66 eV at 100 GPa [Fig. 7(a)]. Pressure constrains Li$^+$ mobility by narrowing the diffusion channels in Li$_2$O. The same effect has also been observed in LiFePO$_4$ and Li$_4$Ti$_5$O$_{12}$ at high pressures [39,56]. The MSDs of Li$^+$ at 1700 K present significant reducing with increasing pressure [Fig. 7(b)]. Over one order of magnitude decrease in Li$^+$ diffusion coefficient is observed as the pressure increases from 0 to 30 GPa (Fig. S8). Thus, elastic stiffening effect under pressure can be intensified in a superionic material due to the confinement of ionic mobility with increasing pressure.

IV. CONCLUSION

Superionic transition in Li_2O takes places at temperatures above $\sim$1300 K. The highly diffusive Li^+ at high temperature leads to significant local structure evolution, which brings profound influence on the elasticity of Li_2O. The calculated elastic properties using the AIMD method show quite good consistency with previous experimental results, and the anomalous softening of C_{11} was observed above $\sim$1300 K. Our results also suggest that anharmonic vibration due to the high mobility of Li^+ is significant in Li_2O before the superionic transition. Therefore, the AIMD method is able to describe the elasticity of materials with fast diffusion elements accurately. In our future research, the ionic transport and elastic properties of other lithium ceramics will be studied, which is essential for these materials used in nuclear fusions

and energy storage devices. The lithium diffusion and elastic properties of Li_2O at high pressure and temperature are also investigated by CINEB and AIMD simulations. We found pressure has negative effects on Li^+ migration, and the elastic stiffening behavior is enhanced in superionic Li_2O with increasing pressure.

[1] C. Johnson and G. Hollenberg, J. Nucl. Mater. **123**, 871 (1984).

[2] S. C. Cowley, Nat. Phys. **12**, 384 (2016) .

[3] C. E. Johnson, K. Noda, and N. Roux, J. Nucl. Mater. **258–263**, 140 (1998).

[4] N. Roux, C. Johnson, and K. Noda, J. Nucl. Mater. **191**, 15 (1992).

[5] D. Fasel and M. Q. Tran, Fusion Eng. Des. **75**, 1163 (2005).

[6] S. T. Murphy, P. Zeller, A. Chartier, and L. V. Brutzel, J. Phys. Chem. C **115**, 21874 (2011).

[7] S. Hull, T. W. D. Farley, W. Hayes, and M. T. Hutchings, J. Nucl. Mater. **160**, 125 (1988).

[8] T. Oda and S. Tanaka, J. Nucl. Mater. **386–388**, 1087 (2009).

[9] H. Pfeiffer, J. Sánchez-Sánchez, and L. J. Álvarez, J. Nucl. Mater. **280**, 295 (2000).

[10] R. Weiyi, W. Feng, Z. Zhou, X. Pingchuan, and S. Weiguo, J. Nucl. Mater. **404**, 116 (2010).

[11] Z. Yuan, X. Kong, S. Ma, T. Gao, C. Xiao, X. Chen, and T. Lu, J. Nucl. Mater. **513**, 232 (2019).

[12] X.-F. Li, X.-R. Chen, C. M. Meng, and G.-F. Ji, Solid State Commun. **139**, 197 (2006).

[13] A. R. Raffray, M. Akiba, V. Chuyanov, L. Giancarli, and S. Malang, J. Nucl. Mater. **307**, 21 (2002).

[14] J. Tiliks, G. Kizane, A. Vitins, G. Vitins, and J. Meistars, Fusion Eng. Des. **69**, 519 (2003).

[15] G. W. Hollenberg, J. Nucl. Mater. **123**, 896 (1984).

[16] A. Suzuki, M. Yamawaki, M. Yasumoto, and K. Yamaguchi, J. Nucl. Mater. **233–237**, 1452 (1996).

[17] R. E. Avila, L. A. Peña, and J. C. Jiménez, J. Nucl. Mater. **405**, 244 (2010).

[18] Y. Oishi, Y. Kamei, and M. Akiyama, J. Nucl. Mater. **87**, 341 (1979).

[19] M. Akiyama, K. Ando, and Y. Oishi, Solid State Ion. **3-4**, 469 (1981).

[20] M. K. Gupta, P. Goel, R. Mittal, N. Choudhury, and S. L. Chaplot, Phys. Rev. B **85**, 184304 (2012).

[21] P. Goel, N. Choudhury, and S. L. Chaplot, Phys. Rev. B **70**, 174307 (2004).

[22] R. Asahi, C. M. Freeman, P. Saxe, and E. Wimmer, Model. Simul. Mater. Sci. Eng. **22**, 075009 (2014).

[23] A. D. Mulliner, P. C. Aeberhard, P. D. Battle, W. I. F. David, and K. Refson, Phys. Chem. Chem. Phys. **17**, 21470 (2015).

[24] R. Fracchia, G. Barrera, N. Allan, T. Barron, and W. Mackrodt, J. Phys. Chem. Solids **59**, 435 (1998).

[25] M. Hayoun, M. Meyer, and A. Denieport, Acta Mater. **53**, 2867 (2005).

[26] M. Hayoun and M. Meyer, Acta Mater. **56**, 1366 (2008).

[27] Y. Duan and D. C. Sorescu, Phys. Rev. B **79**, 014301 (2009).

[28] J. H. Strange, S. M. Rageb, A. V. Chadwick, K. W. Flack, and J. H. Harding, J. Chem. Soc.: Faraday Trans. **86**, 1239 (1990).

[29] T. W. D. Farley, W. Hayes, S. Hull, and R. Ward, Solid State Ion. **28–30**, 189 (1988).

[30] H. Matzke, *Applied Research Reports* (Harwood, London, 1987).

[31] G. Kresse and J. Furthmüller, Phys. Rev. B **54**, 11169 (1996).

[32] W. Kohn and L. J. Sham, Phys. Rev. **140**, A1133 (1965).

[33] P. Hohenberg and W. Kohn, Phys. Rev. **136**, B864 (1965).

[34] D. M. Ceperley and B. J. Alder, Phys. Rev. Lett. **45**, 566 (1980).

[35] J. P. Perdew and A. Zunger, Phys. Rev. B **23**, 5048 (1981).

[36] G. B. Henkelman, P. Uberuaga, and H. Jonsson, J. Chem. Phys. **113**, 9901 (2000).

[37] See Supplemental Material at http://link.aps.org/supplemental/10.1103/PhysRevB.103.174105 for structural properties, Li^+ diffusion coefficients and conductivities, melting temperature, and sound velocities at elevated temperature and pressure.

[38] S. Nosé, J. Chem. Phys. **81**, 511 (1984).

[39] Y. Huang, Y. He, H. Sheng, X. Lu, H. Dong, S. Samanta, H. Dong, X. Li, D. Y. Kim, H.-K. Mao, Y. Liu, H. Li, H. Li, and L. Wang, Nat. Sci. Rev. **6**, 239 (2019).

[40] Y. He, Y. Sun, X. Lu, J. Gao, H. Li, and H. Li, Geophys. Res. Lett. **43**, 6228 (2016).

[41] B. Martorell, L. Vočadlo, J. Brodholt, and I. G. Wood, Science **342**, 466 (2013).

[42] S. Sun, Y. He, D. Y. Kim, and H. P. Li, Phys. Rev. B **102**, 104108 (2020).

[43] D. Alfè, Phys. Rev. B **68**, 064423 (2003).

[44] D. Alfè, Phys. Rev. B **79**, 060101(R) (2009).

[45] S. A. Bonev, E. Schwegler, T. Ogitsu, and G. Galli, Nature (London) **204**, 669 (2004).

[46] T. Ogitsu, E. Schwegler, F. Gygi, and G. Galli, Phys. Rev. Lett. **91**, 175502 (2003).

[47] D. Alfè, C. Cazorla, and M. J. Gillan, J. Chem. Phys. **135**, 024102 (2011).

[48] A. B. Belonoshko, N. V. Skorodumova, A. Rosengren, and B. Johansson, Phys. Rev. B **73**, 012201 (2006).

[49] T. Oda, Y. Oya, S. Tanaka, and W. J. Weber, J. Nucl. Mater. **367–370**, 263 (2007).

[50] W. Voigt, in *Lehrbuch der kristallphysik[M]* (Teubner, Leipzig, 1928), p. 962.

[51] A. Reuss, Z. Angew. Math. Mech. **9**, 49 (1929).

[52] D. Anderson, *Theory of the Earth* (Blackwell Scientific, Boston, 1989).

[53] B. Karki, L. Stixrude, S. Clark, M. Warren, G. Ackland, and J. Crain, Am. Mineral. **82**, 51 (1997).

[54] D. Mainprice, R. Hielscher, and H. Schaeben, Geol. Soc. London Spec. Publ. **360**, 175 (2011).

[55] A. K. Sagotra, D. Chu, and C. Cazorla, Phys. Rev. Mater. **3**, 035405 (2019).

[56] H. Dong, H. Guo, Y. He, J. Gao, W. Han, X. Lu, S. Yan, K. Yang, H. Li, D. Chen, and H. Li, Solid State Ion. **301**, 133 (2017).